CHEMISTRY OF MATERIALS

pubs.acs.org/cm

Article



# Superconducting High-Pressure Forms of LiSi and LiGe Featuring Square Planar Nets

*Published as part of Chemistry of Materials special issue "Honoring the Outstanding Contributions of Mercouri Kanatzidis to Chemistry of Materials".*

Doreen C. Beyer, Kristina Spektor, Roman Lucrezi, Pedro Nunes Ferreira, Christoph Heil, Shrikant Bhat, Robert Farla, Volodymyr Baran, Martin Aaskov Karlsen, Martin Etter, Vanessa Stephan, Martin Boerner, Christopher Owen, Andrew J. Morris, Holger Kohlmann, and Ulrich Häussermann*

Cite This: https://doi.org/10.1021/acs.chemmater.5c02061

Read Online

ACCESS | Metrics & More | Article Recommendations | Supporting Information

**ABSTRACT:** High-pressure forms of LiX (X = Si or Ge) that adopt the simple tetragonal *P*4/*mmm* CuAu structure were synthesized by reacting stoichiometric $Li_{12}Si_7$/5Si mixtures and by transforming $I4_1/a$-LiGe (MgGa structure) at ~12.5 GPa and 410 and 265 °C, respectively. *P*4/*mmm*-LiGe was recovered in quantitative yield as a metastable phase at ambient pressure, whereas *P*4/*mmm*-LiSi was partially converted into a hitherto unknown, kinetically more stable polymorph. The structures of the *P*4/*mmm* phases consist of alternately stacked square planar nets of X ($d_{Si-Si}$ = 2.595 Å, and $d_{Ge-Ge}$ = 2.761 Å) and Li atoms. Density functional theory (DFT)-based electronic structure calculations reveal pronounced polarity, $Li^{0.83+}Si^{0.83-}$ and $Li^{0.84+}Ge^{0.84-}$, together with strong covalent bonding between X atoms. Electron−phonon coupling calculations within the Migdal−Eliashberg framework predict superconducting transition temperatures of ~7 K for *P*4/*mmm*-LiGe and ~6 K for *P*4/*mmm*-LiSi. For LiGe, magnetic susceptibility measurements show a sharp diamagnetic transition at 6.3 K, in support of the theoretical result.

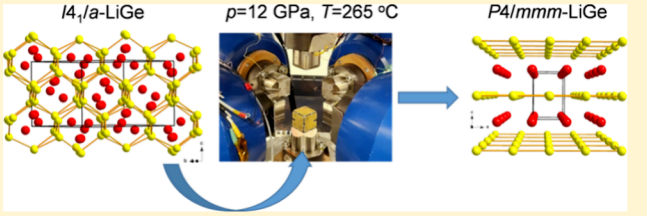


## INTRODUCTION

The presence of square ($4^4$) nets of atoms in crystal structures is associated with interesting properties, most notably superconductivity (e.g., square nets in cuprate and iron-based superconductors)[1−3] and lately exotic properties within the concept of topological semimetals.[4−7] Square net materials typically crystallize in tetragonal structures, with the $4^4$ nets embedded between building blocks of varying complexity. In most cases, these nets are side-centered with respect to the tetragonal base of the square net material such that $d_{square} = 1/\sqrt{2}a_{tet}$.[7] The most elementary square net structure, however, is expressed with the intermetallic CuAu structure type (*P*4/*mmm*), which relates to the fcc structure for *c*/*a* values of around $\sqrt{2}$ (for CuAu, *c*/*a* = 1.305) or to the CsCl (bcc) structure when *c*/*a* is closer to 1 (cf. Figure 1). In the inorganic crystal structure database (ICSD),[8] the latter case is distinguished as the CuTi structure type (for CuTi, *c*/*a* = 1.15). Among the CuAu-structured intermetallics, one can identify a small group of polar representatives, consisting of an "active" (reducing) metal (alkali, alkaline earth, or lanthanide) and a p element (X), such as LiBi, NaBi, CaPb, YbSn, YbPb, EuIn, YbGa, and GdIn.[8] In these systems, substantial charge transfer from the active metal and covalent bonding between formally reduced X atoms are expected. As a result, the square net would become an electronically distinct two-dimensional

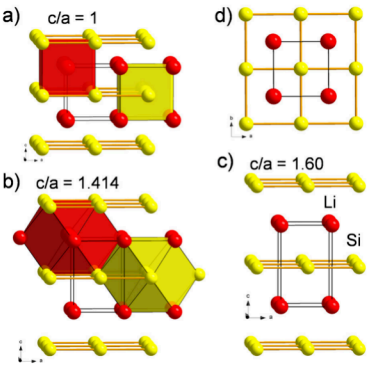


**Figure 1.** Variations of the tetragonal CuAu structure type (*P*4/*mmm*). (a) *c*/*a* close to 1, related to bcc (CsCl) (frequently designated as the CuTi structure type). b) *c*/*a* close to $\sqrt{2}$, related to fcc. Representatives typically do not have *c*/*a* ratios that exceed $\sqrt{2}$. (c) Crystal structure of LiSi with a *c*/*a* ratio of ≈1.6. (d) Projection of the CuAu structure along the [001] tetragonal direction.

Received: August 4, 2025
Revised: January 10, 2026
Accepted: January 13, 2026

polyanion, stabilized by the surrounding nets of active metal ions.

The electronic structure of a square net built of X atoms (i.e., involving only s and p orbitals) has been analyzed numerous times.[9−11] Depending on the specific p element, the extent of s−p mixing, the strength of $\pi$-type interaction between p orbitals, and the degree of p band filling can vary substantially. Together, these factors give rise to good metallic behavior, characterized by a high density of states at the Fermi level. An $(s^2)p^3$ electron configuration provides an optimum bonding situation (with roughly half-filled p bands).[6,7] However, regardless the degree of p band filling, the square net is inherently unstable, at least at low temperatures, with respect to structural (Peierls) distortions.[12] If the net is found to be stable, then most likely a magnetic or superconducting state is present, which reduces the total energy of the electronic system. Indeed, LiBi and NaBi were shown to be superconductors, although with modest transition temperatures $T_c$ (2−2.5 K).[13,14] Assuming electron transfer from Li, Bi acquires a formal $p^4$ electron configuration (or rather $p_{3/2}{}^2$), which implies the population of antibonding states. The band structure of a square net built of Bi atoms is special because relativistic effects will cause a largely detached s band and split $p_{1/2}/p_{3/2}$ bands.[14]

In this study, we focus on LiSi and LiGe. The X atoms are comparatively light and formally attain a $p^3$ electron configuration. Thus, one would expect strong covalent bonding within square nets and, because of the smaller size of X, significant $\pi$-interaction. From density functional theory (DFT) calculations, LiSi and LiGe have been predicted to attain the *P*4/*mmm* CuAu structure at pressures above 2.5−3.3 and 5 GPa, respectively.[15,16] Under ambient conditions, LiSi and LiGe adopt the same ground state structure (MgGa structure type, $I4_1/a$)[17,18] and follow the Zintl−Klemm concept according to which an electron transfer from Li is assumed, leading to reduced X atoms ($X^-$), which polymerize into a 3-bonded polyanionic X network in order to achieve an octet (Figure S1a and Table S1). While LiGe can be readily synthesized via fusion of the elements, the formation of LiSi is kinetically hindered.[19] Previous work has shown that these kinetic barriers can be overcome through ball milling[20] or by applying moderate pressures (1−4 GPa).[17,21] For LiGe, high-pressure treatments near 4 GPa led to the discovery of several polymorphs (cf. Figure S1b,c and Table S1), but none corresponded to the predicted *P*4/*mmm* phase.[22,23] Consequently, experimental results for LiSi and LiGe at pressures of up to 4 GPa starkly vary from the theoretical predictions.

Here, we report on the synthesis of *P*4/*mmm*-LiSi and *P*4/*mmm*-LiGe at pressures above 10 GPa and the characterization of the materials after recovery to ambient conditions. Electronic structure and electron−phonon coupling calculations confirm the presence of covalently bonded $4^4$ nets and predict superconductivity in both compounds. For LiGe, this prediction could be supported by magnetic susceptibility measurements.

## 2. MATERIALS AND METHODS

### Synthesis of Precursors

$I4_1/a$-LiGe was obtained by fusion of a stoichiometric mixture of Li (99.9%, Alfa Aesar) and Ge (99.999%, Smart Elements) in a Nb crucible that was sealed in a silica ampule.[18,24] As ball-milling equipment was not available for $I4_1/a$-LiSi synthesis, we employed a stoichiometric mixture of $Li_{12}Si_7$[25] and Si (1:5) as a precursor. $Li_{12}Si_7$ was synthesized from the elements according to the method described by Thomas et al.[26] Si powder (99.9999%, ABCR GmbH) and an excess of 5 mol % Li (99.9%, Onyxmet) were sealed in a Ta ampule that was heated in vacuum at 750 °C (120 °C/h) for 1.5 h, and then the reaction was quenched in air to room temperature. The sample was annealed afterward at 450 °C for 24 h. The phase purity of the precursors was confirmed by powder X-ray diffraction (cf. Figures S2 and S3).

### High-Pressure Experiments

All steps of sample preparation for high-pressure experiments were performed in an Ar-filled glovebox. The starting materials ($I4_1/a$-LiGe and $Li_{12}Si_7$/5Si (99.9999%, ABCR GmbH) mixture) were compressed into pellets (1.5 mm outside diameter (OD); $h \approx 1.75$ mm) and sealed in NaCl capsules (3 mm OD; $h \approx 3$ mm). The samples were compressed to pressures between 12 and 12.5 GPa using the large volume press (LVP) Aster-15 at beamline P61B, DESY,[27] and employing 14/7 multianvil assemblies with a graphite heater.[28] Heating was performed with an AC power supply. The sample temperature was approximated from a precalibrated heater power−temperature relationship based on type C thermocouples (estimated $T$ uncertainty of <20 K).

*In situ* investigations utilized energy dispersive X-ray diffraction (EDXRD). EDXRD patterns were acquired by using two Ge detectors positioned at $2\theta$ values of ≈2.9895° and ≈5.0022° to access a wider range of $d$ spacings. Data were collected during compression and heating after exposure time for 100 s. The pressure was determined from NaCl reflections of the sample capsule and using the NaCl equation of state (EOS) of Matsui et al.[29] (estimated $p$ uncertainty of ±0.2 GPa). The *in situ* EDXRD data were initially evaluated and handled using PDIndexer,[30] and for indexing, the TAUP algorithm[31] of the CRYSFIRE suite[32] was employed. Lattice parameters were determined from Le Bail analysis[33] in GSAS-II.[34]

Off-line (*ex situ*) high-pressure experiments followed the same setup that was used for the *in situ* investigations. Applied loads corresponded to a pressure of ∼12.5 GPa. Heating to 600 °C over 70 min was followed by annealing for 2 h, cooling to room temperature (RT) within ∼15 min, and subsequent decompression. The products from both *in situ* and *ex situ* high-pressure experiments were recovered in an Ar-filled glovebox. As shown in Figure S6, initially recovered samples corresponded to dark gray sintered pellets. Broken pieces displayed metallic luster.

### *Ex Situ* Powder X-ray Diffraction (PXRD) Characterization of Products

PXRD patterns of recovered LiSi and LiGe samples were collected at beamline P02.1, PETRA III, DESY,[35] using monochromatic synchrotron radiation ($E \approx 60$ keV; $\lambda$ = 0.20734, 0.20738, and 0.20740 Å at the three different occasions of measurements). Samples were broken apart and sealed (as sintered pieces without grinding) inside 1.0 mm diameter capillaries. For variable-temperature measurements, fused silica capillaries were heated with a mini hot air blower, which is one of the sample environments available at P02.1. Rietveld refinement of the PXRD data was performed using FullProf.[36] Further details are provided in the Supporting Information.

### Magnetic Property Measurements

Magnetic susceptibility measurements were performed by using a SQUID magnetometer (Quantum Design MPMS 7XL). A lightly crushed sample (1−3 mg) was placed in a gelatin capsule that was subsequently mounted in a sample holder straw under dry argon. The sample was cooled in the absence of a magnetic field. After the introduction of a 10 G field, magnetic data were recorded while the sample was warmed ("diamagnetic shielding") and then cooled ("Meissner effect").

### Computational Details

DFT calculations utilized the Quantum ESPRESSO (QE) package.[37−39] Vibrational properties were calculated within density functional perturbation theory (DFPT),[40] using optimized norm-conserving Vanderbilt (ONCV) pseudopotentials[41,42] in combination


https://doi.org/10.1021/acs.chemmater.5c02061
Chem. Mater. XXXX, XXX, XXX−XXX

with the PBE[43] exchange-correlation functional. The kinetic energy cutoff for the wave functions was set to 80 Ry, and the convergence threshold for the electronic self-consistency to $10^{-10}$ Ry. A Methfessel–Paxton smearing[44] value of 0.02 Ry was used for the metallic occupation numbers. For the self-consistent field calculations, we adopted an unshifted 18 × 18 × 12 k-grid for the *P*4/*mmm* structures in the conventional tetragonal unit cell containing two atoms and an unshifted 10 × 10 × 10 k-grid for the $I4_1/a$ structures in the primitive body-centered tetragonal unit cell containing 16 atoms. These settings provide a numerical accuracy for the total energy on the order of 1 meV/atom with respect to selected reference calculations with an energy cutoff of 300 Ry and a k-grid tripled along each reciprocal lattice vector.

The phonon self-consistency threshold was set to $10^{-16}$, and the phonon and electron–phonon quantities were calculated on 6 × 6 × 4 q-grids. The electron–phonon matrix elements were integrated over a denser 54 × 54 × 36 k-grid and evaluated for 30 double-delta smearing values in the range of 0.001–0.030 Ry, where a value of 0.020 Ry was chosen for the presented results in combination with a phonon smearing value of 0.2 THz for the q-grid integration. The calculated Eliashberg function and density of states (DOS) were then used to solve the isotropic Migdal–Eliashberg (ME) equations using the IsoME package[45] and applying a typical $\mu^*$ value of 0.1 for the Morel–Anderson pseudopotential.[46] The ME $T_c$ values represent the temperatures at which the superconducting gaps vanish.[47] The ME equations are solved in two different flavors, namely, in the constant-DOS approximation and in the full-bandwidth formulation, and both approaches result in the same $T_c$. The DOS were calculated on k-grids tripled along each reciprocal lattice vector and using the tetrahedron method for the metallic occupations.

Bader analysis of electron densities was carried out within the Critic2 package[48,49] using the YT approach[50] and the Henkelman group approach.[51−53] Electron localization functions (ELF) and charge densities were calculated within QE's postprocessing tools and plotted using VESTA.[54] The charge densities needed for the Bader analysis were calculated using kjPAW[55] pseudopotentials from the PSLibrary[56] with a kinetic energy cutoff of 120 Ry for the wave functions and 960 Ry for the charge density.

## 3. RESULTS

Although theoretical studies predicted that *P*4/*mmm*-LiSi and *P*4/*mmm*-LiGe should form at relatively low pressures, previous experimental work demonstrated that applying pressures of up to 4 GPa is insufficient to obtain these phases.[17,21−23] Our initial experiments (see the Supporting Information) similarly indicated that pressures above 10 GPa are required (Figures S4 and S5). Indeed, synthesis attempts at ∼12.5 GPa and 600 °C yielded *P*4/*mmm*-LiX. However, samples recovered to ambient pressure contained a secondary phase: minor in LiGe and substantial in LiSi (Figures S7 and S8). Subsequent *in situ* experiments then provided deeper insight into the formation conditions of *P*4/*mmm*-LiSi and *P*4/*mmm*-LiGe.

Figure 2a presents the evolution of EDXRD patterns of the $Li_{12}Si_7$/5Si reaction mixture during heating at 12.3 GPa. At around 100 °C, Si began transforming into the Si-II (*β*-Sn) phase. At ∼225 °C, reflections of *P*4/*mmm*-LiSi appeared. Concurrently, reflections of an unidentified additional phase ($d$ = 4.28 and 2.14 Å) emerged, although their intensities did not noticeably increase with further heating. Reflections from the starting materials disappeared at 325 °C, and the reflections of the unidentified phase vanished upon annealing at 410 °C. At this stage, the pattern corresponded to phase-pure *P*4/*mmm*-LiSi. Upon cooling to RT, the pressure decreased to 11.7 GPa while the sample remained in the single-phase *P*4/*mmm*-LiSi phase. However, after complete pressure release,

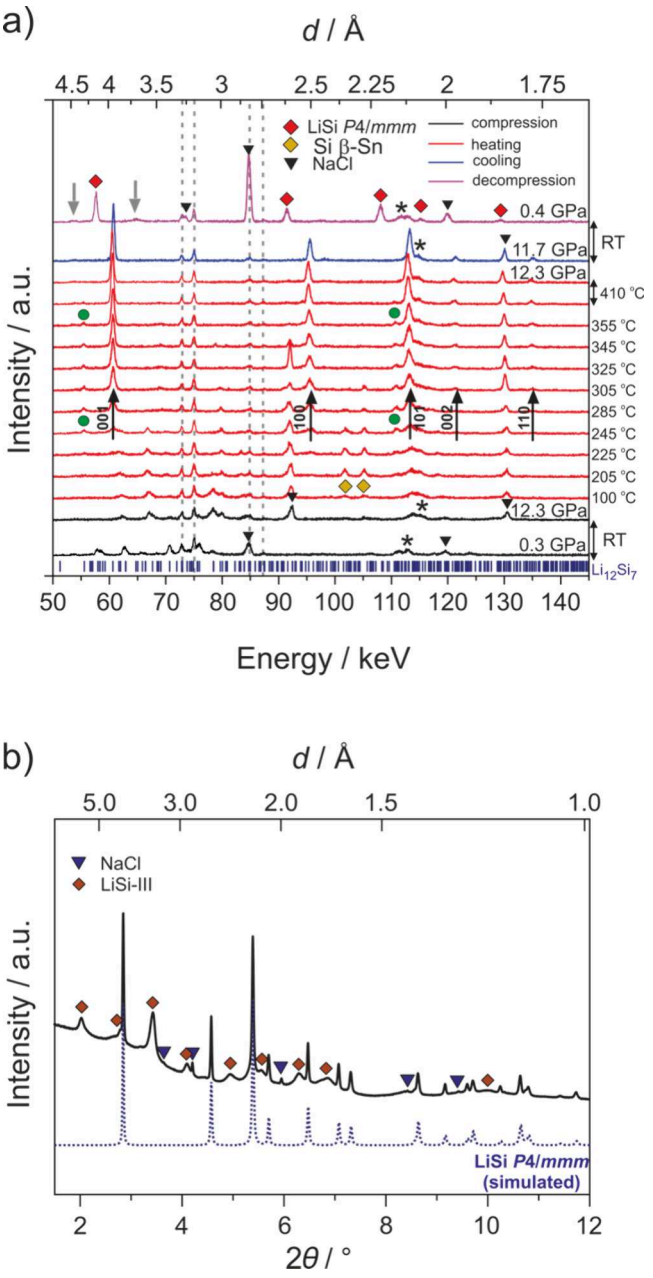


**Figure 2.** (a) Diffraction patterns acquired for the $Li_{12}Si_7$/5Si mixture compressed to 12.3 GPa (black) and subsequently heated to 410 °C (red), cooled to room temperature (blue), and decompressed to nearly ambient pressure (violet) at $2\theta \approx 3.0°$. The formation of *P*4/*mmm*-LiSi is indicated by black arrows. Reflections of *P*4/*mmm*-LiSi, Si-II (*β*-Sn structure), and the salt capsule are marked with red diamonds, yellow diamonds, and black triangles, respectively. Reflections from an unknown, intermediate phase are marked with green circles. Secondary Pb fluorescence peaks (from the detector shielding) are marked as dashed gray vertical lines. A broad reflection, marked with an asterisk, stems from MgO, which is a part of the pressure cell assembly. Broad and weak reflections in the pattern after decompression are marked with gray arrows. (b) Synchrotron PXRD pattern ($\lambda$ = 0.20735(1) Å) of the product from the $Li_{12}Si_7$ + 5Si reaction at 12.3 GPa and 410 °C (panel a), revealing a mixture of *P*4/*mmm*-LiSi and LiSi-III.

weak and broad additional reflections became visible. Figure 2b displays the PXRD pattern of the recovered sample (measured ∼2 weeks after the *in situ* experiment), which was virtually


https://doi.org/10.1021/acs.chemmater.5c02061
Chem. Mater. XXXX, XXX, XXX−XXX

Table 1. Crystallographic Data for *P*4/*mmm*-LiX under Ambient Conditions (Li on 1a (0, 0, 0), X on 1d (1/2, 1/2, 1/2))

| | $a$ (Å) | $c$ (Å) | $c/a$ | $V$ (Å$^3$) | $\rho$ (g/cm$^3$) | $d_{X-X}$ (Å) | $d_{Li-X}$ (Å) |
|---|---|---|---|---|---|---|---|
| LiSi | 2.5951(2) | 4.1665(4) | 1.606 | 28.058(3) | 2.072(1) | 2.5951(1) | 2.7762(2) |
| LiGe | 2.76081(2) | 4.15115(4) | 1.504 | 31.6404(4) | 4.175(1) | 2.7608(1) | 2.8494(1) |

identical to the pattern from the off-line synthesis product obtained at 600 °C (cf. Figure S7). Both samples exhibit a substantial fraction of a secondary phase with characteristic broad reflections. Table 1 summarizes the lattice parameters and interatomic distances of *P*4/*mmm*-LiSi under ambient conditions. A collection of lattice parameters at high pressure and temperature is provided in Table S2.

From this experiment, we infer that *P*4/*mmm*-LiSi exhibits a rather low kinetic stability. Instead of directly reverting into the ground state ($I4_1/a$-LiSi), it transformed over time into a hitherto unknown polymorph, here termed LiSi-III. The broad reflections suggest either a very small crystallite size or a high degree of structural disorder. Upon heating the recovered sample at ambient pressure, *P*4/*mmm*-LiSi began to transition above ∼100 °C, while the broad Bragg peaks of LiSi-III sharpened and intensified (Figures S9−S11). A preliminary structural characterization of LiSi-III is presented in Figure S16 and Table S7. At temperatures above 250 °C, the onset of transformation to ground state $I4_1/a$-LiSi was observed, and LiSi-III completely converted into $I4_1/a$-LiSi at approximately 330 °C.

Figure 3a shows the evolution of the EDXRD patterns for $I4_1/a$-LiGe during heating at 12.4 GPa. Around 100 °C, $I4_1/a$-LiGe began to transform into a previously unknown polymorph, indexed here as *P*2/*m*-LiGe (isostructural with LiSn (cf. Table S3)). Upon annealing at 210 °C, reflections of *P*4/*mmm*-LiGe became apparent. The *P*2/*m* phase remained stable up to 245 °C but vanished during annealing at this temperature. A clean *P*4/*mmm*-LiGe pattern was obtained at 265 °C and remained unchanged after cooling and subsequent decompression. The PXRD pattern of the recovered sample (Figure 3b) confirms the formation of nearly phase-pure *P*4/*mmm*-LiGe. However, a few tiny reflections coincided with those of the secondary phase (designated here as LiGe-V) previously found in the product synthesized at 600 °C (Figure S8). In contrast to the LiSi analogue, the *P*4/*mmm*-LiGe phase appears to be stable over time. The lattice parameters and interatomic distances of *P*4/*mmm*-LiGe under ambient conditions are listed in Table 1, and lattice parameters for high-pressure and -temperature conditions are provided in Tables S2 and S3.

Heating the sample synthesized at 600 °C (containing a substantial fraction of LiGe-V) at ambient pressure resulted in the emergence of reflections associated with ground state $I4_1/a$-LiGe at ∼90 °C. The *P*4/*mmm* phase was completely decomposed above 150 °C (Figures S12−S14). Similar to the behavior observed for LiSi-III, the Bragg peaks of LiGe-V sharpened and intensified upon heating. During annealing at 210 °C, LiGe-V was fully converted into $I4_1/a$-LiGe. Unlike *P*4/*mmm*-LiSi, the LiGe analogue appears to transform directly into the ground state phase rather than via LiGe-V, leaving the origin of LiGe-V unresolved (see the Supporting Information).

Figure 4 presents the result of dc magnetic measurements on the *P*4/*mmm*-LiGe sample in the temperature range of 2−15 K under an applied magnetic field of 10 G. Due to the limited sample mass and the extreme sensitivity of *P*4/*mmm*-LiGe toward moisture, the measurement is primarily qualitative.

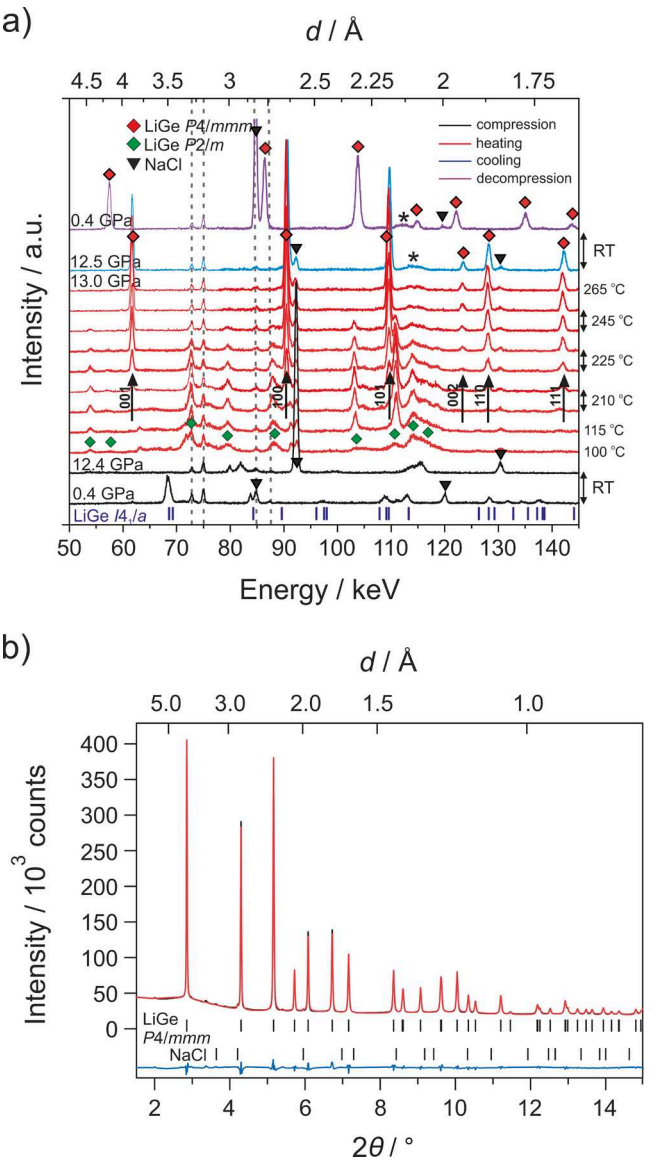


**Figure 3.** (a) Diffraction patterns acquired for $I4_1/a$-LiGe compressed to 12.4 GPa (black) and subsequently heated to 265 °C (red), cooled to room temperature (blue), and decompressed to nearly ambient pressure (violet) at $2\theta \approx 3.0°$. The formation of *P*4/*mmm*-LiGe is indicated by black arrows, and reflections of *P*4/*mmm*-LiGe are marked with red diamonds. Reflections of intermediate *P*2/*m*-LiGe and reflections from the salt capsule are marked with green diamonds and black triangles, respectively. Secondary Pb fluorescence peaks (from the detector shielding) are marked as dashed gray vertical lines. A broad reflection, marked with an asterisk, stems from MgO, which is a part of the pressure cell assembly. (b) Rietveld fit to the synchrotron PXRD pattern ($\lambda$ = 0.20735(1) Å) of the product from $I4_1/a$-LiGe conversion at 12.4 GPa and 265 °C (panel a). $R_p$ = 3.0%. $R_{wp}$ = 4.14%. $R_{exp}$ = 0.76%. For *P*4/*mmm*-LiGe, $R_f$ = 1.23% and $R_{Bragg}$ = 2.45%.

Nevertheless, the data provide clear evidence of superconductivity. After zero-field cooling below the critical


https://doi.org/10.1021/acs.chemmater.5c02061
Chem. Mater. XXXX, XXX, XXX−XXX

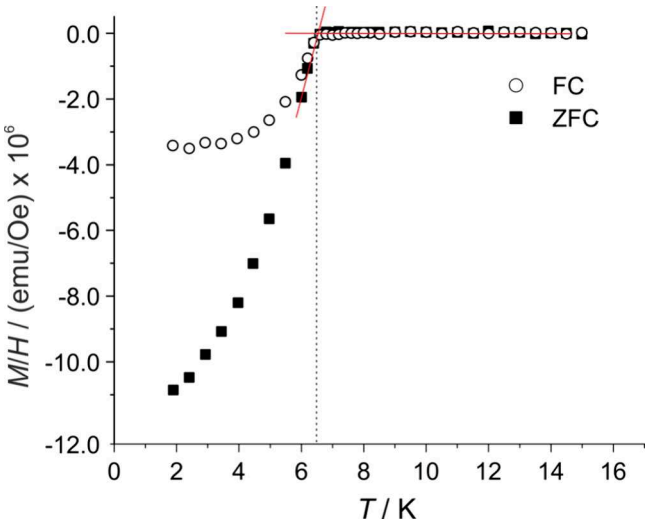


**Figure 4.** Magnetic behavior of *P*4/*mmm*-LiGe at low temperatures: field-cooled (○) and zero-field-cooled (■) at 10 G.

temperature ($T_c$), warming under applied fields yields negative susceptibility values characteristic of diamagnetic shielding. Diamagnetism is suppressed above a $T_c$ of approximately 6.5 K. This trend is retained upon cooling under an applied magnetic field, consistent with a Meissner response. The magnetic behavior of *P*4/*mmm*-LiGe is, therefore, consistent with that of a type II superconductor. Full characterization of superconducting will require complementary electrical transport and heat capacity measurements. A corresponding measurement for *P*4/*mmm*-LiSi could not be achieved due to its limited temporal stability (Figure S7).

## 4. DISCUSSION

Metastable *P*4/*mmm*-LiSi and *P*4/*mmm*-LiGe can be synthesized at pressures that can be accessed with large-volume press (LVP) techniques. Unlike diamond anvil cell methods, LVP synthesis enables the production of significantly larger sample quantities suitable for detailed postsynthetic characterization. However, successful synthesis requires precise knowledge of narrow $p-T$ formation windows dictated by complex polymorphic phase relations, and recovery is further complicated by the low kinetic stability of these phases. While *P*4/*mmm*-LiGe can be recovered as a phase-pure sample at ambient pressure, it remains uncertain whether this can be achieved as well for *P*4/*mmm*-LiSi.

At ambient pressure, the densities of *P*4/*mmm*-LiSi (2.072 g/cm$^3$) and *P*4/*mmm*-LiGe (4.175 g/cm$^3$) exceed those of their $I4_1/a$ ground state analogues (1.851 and 3.782 g/cm$^3$, respectively) by 10−12% (Table 1). The interatomic X−X distances within the square planar nets are 2.595 Å (Si) and 2.761 Å (Ge). Relative to the 3-bonded networks in the corresponding ground state phases (LiSi, 2.417 Å × 2 and 2.502 Å (average of 2.445 Å); LiGe, 2.554 Å × 2 and 2.601 Å (average of 2.570 Å)), these values represent an average elongation of roughly 7%. The $c/a$ ratios for *P*4/*mmm*-LiSi (1.606) and *P*4/*mmm*-LiGe (1.504) are markedly larger than $\sqrt{2}$, making them the first CuAu-type representatives with such enhanced axial ratios (cf. LiBi = 1.262; NaBi = 1.387).[8] These unusually high $c/a$ values likely reflect strong covalent bonding interaction between square net-forming X atoms, which drives contraction of the $a$ lattice parameter.

The structural parameters of the *P*4/*mmm*-LiX phases are accurately reproduced by our DFT calculations (Table 2).

**Table 2. Calculated Structure Parameters and Properties for the *P*4/*mmm*-LiX Phases[a]**

| | *P*4/*mmm*-LiSi | *P*4/*mmm*-LiGe |
|---|---|---|
| $a$ (Å) | 2.597 | 2.789 |
| $c$ (Å) | 4.118 | 4.103 |
| $c/a$ | 1.59 | 1.47 |
| Bader charge $z$ (e) | 0.828/−0.828 | 0.838/−0.838 |
| Bader volume of Li (Å$^3$) | 23.6 | 25.4 |
| Bader volume of X (Å$^3$) | 163.8 | 190.1 |
| $\lambda$ | 0.55 | 0.75 |
| $\omega_{log}$ (meV) | 28 | 15 |
| $N(E_F)$ (eV$^{-1}$) (%X) | 0.52 (96) | 0.60 (97) |
| $T_c$(ME) (K) | 6 | 7 |

[a]For the $I4_1/a$ ground state phases, see Figures S23 and S24 and Table S8.

Figure 5 shows the electronic band structure and atom-projected DOS, which appear broadly similar at first glance. As expected for Zintl phases, the occupied states are dominated by contributions from the X atoms. Notably, the $p_z$ and $p_{xy}$ bands do not mix along high-symmetry lines, which simplifies the analysis of the band structures: The $p_z$ band dispersion along the Γ−X path reflects the strength of $\pi$-interactions within square nets; the behavior at point M provides insight into the degree of s−$p_{xy}$ mixing, and the dispersion of the second band along the Γ−Z path (mixed $p_z$−$s_{Li}$) indicates the interaction strength between nets.[10]

Although the energy positions of the s band minimum are nearly identical in both LiSi and LiGe, its dispersion is significantly larger in LiSi. This results in an avoided crossing with the $p_{xy}$ bands at M, signaling strong s−p mixing. By contrast, the s and p bands in LiGe remain clearly separated. The $p_z$ band dispersion along the Γ−X path is ∼4.2 eV for LiSi and ∼3.6 eV for LiGe, indicating stronger $\pi$-interactions in LiSi. Interestingly, the inter-net interaction appears more pronounced in LiGe, as reflected in the larger dispersion of the second Γ−Z band (∼2.3 eV vs ∼2.0 eV for LiSi), which may correlate with its smaller $c/a$ ratio. Small differences also appear in the vicinity of the Fermi level, particularly along the A−Z path. The DOS at the Fermi level, $N(E_F)$, is slightly higher for LiGe (0.6 state eV$^{-1}$ formula unit$^{-1}$) than for LiSi (0.52 state eV$^{-1}$ formula units$^{-1}$) (Table 2).

Figure 6 presents the electron density ($\rho$) and electron localization function (ELF)[57] maps, which support the analysis of the band structures. Bader analysis[58] indicates substantial charge transfer in the *P*4/*mmm* phases, with values of 0.83 and −0.83 (Table 2), essentially identical to those of the $I4_1/a$ Zintl phase ground state structures (0.85 and −0.85 (Table S8)). The Bader volumes for $Li^+$ are comparable in both structure types, whereas those of $X^-$ are considerably smaller in the *P*4/*mmm* phases. The $\rho$ maps show a (3, −1) critical point ("bond critical point")[58] midway between the X atoms, confirming the presence of covalently bonded square nets. Both ELF and $\rho$ attain local minima at the center of the $X_4$ squares (ring critical points) and show low electron density around Li sites, consistent with dominantly ionic Li−X interactions.[59] A notable feature is that ELF maxima ("attractors")[60] in the valence region are not located between two X atoms (or on a line perpendicular to the X−X distances


https://doi.org/10.1021/acs.chemmater.5c02061
Chem. Mater. XXXX, XXX, XXX−XXX

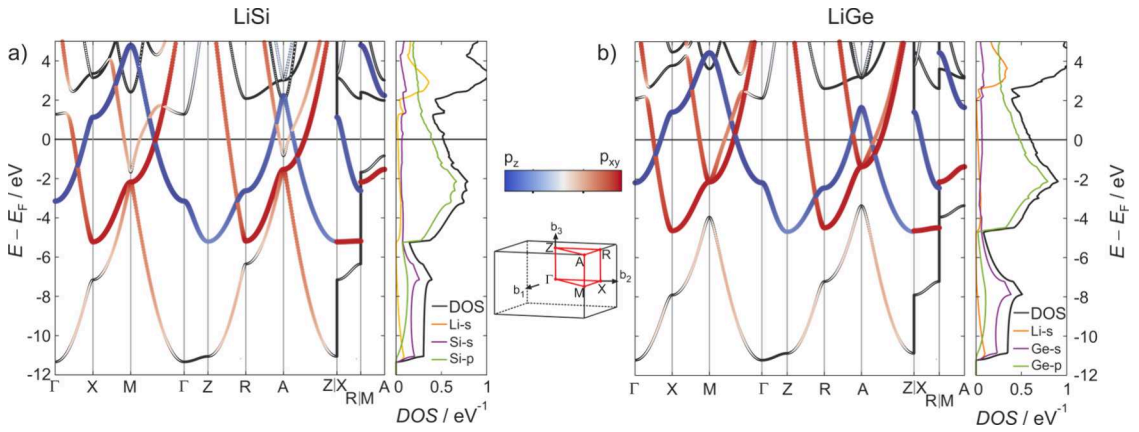


**Figure 5.** Electronic band structure and atom-projected density of states (DOS) for (a) *P*4/*mmm*-LiSi and (b) *P*4/*mmm*-LiGe. The contributions of X atom $p_z$ and $p_{xy}$ orbitals to bands are depicted as "fat bands", colored red and blue, respectively. See Figure S22 for different fat band presentations of the band structures. The Brillouin zone is adapted with permission from ref 61. Copyright 2010 Elsevier.

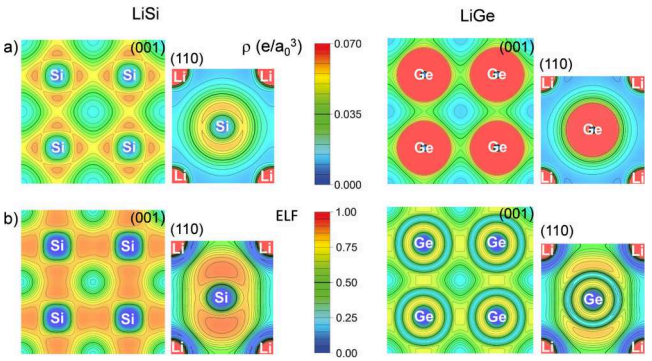


**Figure 6.** (a) Electron density $\rho$ and (b) electron localization function (ELF) plots for the planes (001), containing X atom square nets, and (110) for *P*4/*mmm*-LiSi (left) and *P*4/*mmm*-LiGe (right). The unit for $\rho$ is e per Bohr$^3$ ($a_o \approx 0.52917$ Å). Isolines are plotted in intervals of 0.005 e/$a_o^3$ with the value of 0.0035 highlighted in bold. ELF values are restricted between 0 and 1. Isolines are drawn in intervals of 0.05 with the value of 0.5 highlighted in bold.

and the tetragonal plane, as perhaps expected for $\pi$-bonding) but above and below the X atoms (see also Figure S24a). In contrast, the ELF distribution in the $I4_1/a$ ground state structures aligns with the VSEPR picture of a 3-bonded Si network, displaying three bond attractors and one lone pair attractor (cf. Figure S24b).[60]

Figure 7 shows the phonon dispersion relations, the phonon density of states, $F(\omega)$, the Eliashberg electron−phonon coupling function, $\alpha^2F(\omega)$, and the cumulative electron−phonon coupling constant, $\lambda(\omega)$, for *P*4/*mmm*-LiX, with calculated superconducting parameters included in Table 2. The two atoms in the primitive cell yield three optic and three acoustic phonon modes, with the heavier X atom contributing predominantly to the acoustic modes. Both acoustic and optical dispersions are significantly narrower for LiGe, and the Li- and Ge-derived modes are well separated. The acoustic region (largely X-based vibrations) accounts for ∼90% of the total $\lambda(\omega)$, indicating that coupling between X vibrations and X-derived electronic states is substantially more effective for Ge. This arises from the weaker dispersion of the acoustic modes, which enhances their contribution to $\alpha^2F(\omega)$, together with the higher $N(E_F)$ in LiGe. Although LiSi exhibits a higher logarithmically averaged frequency $\omega_{log}$, for weak-coupling superconductors ($\lambda < 1$) the value of $\lambda$ typically dominates.

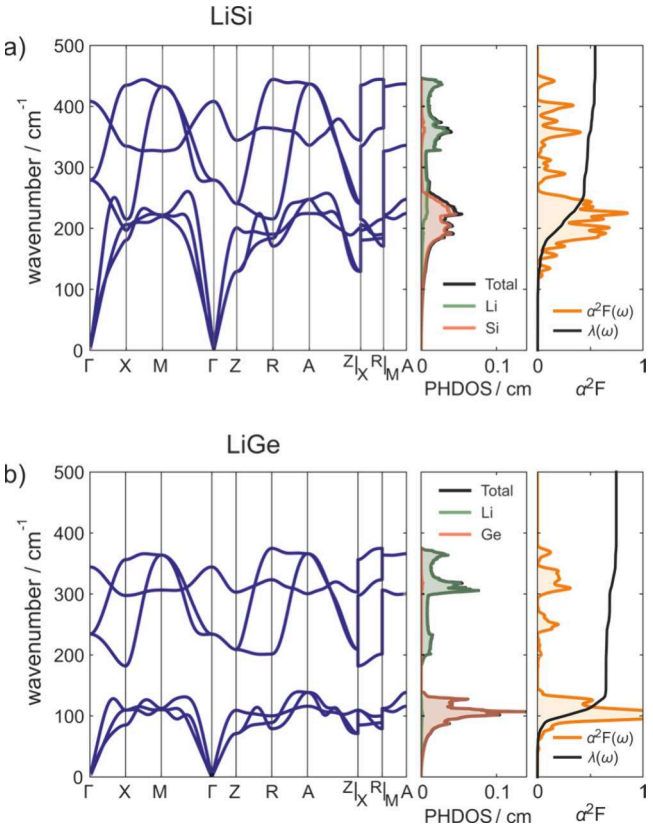


**Figure 7.** Phonon dispersions, phonon density of states (PHDOS) decomposed into atomic contributions, and Eliashberg function $\alpha^2F(\omega)$ (from left to right, respectively) with electron−phonon coupling constant $\lambda(\omega)$ for (a) *P*4/*mmm*-LiSi and (b) *P*4/*mmm*-LiGe.

Even a modest increase in $\lambda$ can lead to significant enhancements in $T_c$, often outweighing the effect of decreased phonon energies.

## 5. CONCLUSIONS

LiSi and LiGe (LiX) display rich polymorphism at moderate pressures. Phases adopting the simple *P*4/*mmm* CuAu-type structure, characterized by square nets of X atoms, can be synthesized at ∼12.5 GPa and comparatively low temperatures (<410 °C). *P*4/*mmm*-LiGe can be recovered as an almost


https://doi.org/10.1021/acs.chemmater.5c02061
Chem. Mater. XXXX, XXX, XXX−XXX

phase-pure material, whereas *P*4/*mmm*-LiSi is obtained only in mixtures containing a previously unknown polymorph, LiSi-III, into which it gradually transforms under ambient conditions. Chemical bonding between square net-forming X atoms is strongly covalent, imparting a distinctly two-dimensional character to the electronic band structure and supporting classification of these compounds as square net materials. However, additional studies are needed to elucidate the expected anisotropic behavior in their electronic and mechanical properties.

Electron−phonon coupling calculations indicate that the *P*4/*mmm*-LiX phases are superconductors with a $T_c$ between 6 and 7 K. The calculations further show that the electron−phonon coupling is dominated by acoustic phonons associated with X atom vibrations. Because the X atoms also provide the primary contributions to the DOS at the Fermi level, we conclude, analogous to the case of the LiBi compound,[14] that superconductivity is primarily rooted in the square nets formed by the X atoms. A comprehensive experimental investigation of the superconducting properties of the *P*4/*mmm*-LiX phases remains an outstanding challenge, owing to their extreme air and moisture sensitivity and, in the case of LiSi, its gradual decomposition under ambient conditions. However, the synthesis conditions developed in the present work provide a viable route to producing larger sample quantities to enable such studies.

## ■ ASSOCIATED CONTENT

### Supporting Information

The Supporting Information is available free of charge at https://pubs.acs.org/doi/10.1021/acs.chemmater.5c02061.

Compilation of selected crystal structures of LiSi and LiGe polymorphs, PXRD characterization of LiGe and $Li_{12}Si_7$ precursors, results from initial high-pressure experiments at ∼10 GPa, details and summary of the PXRD characterization of *P*4/*mmm*-LiX products, detailed description and data evaluation for the multi-temperature synchrotron PXRD experiments on *P*4/*mmm*-LiX, preliminary structural characterization of LiSi-III, and electronic structure calculations for *P*4/*mmm* and $I4_1/a$-LiX (PDF)

### Accession Codes

Deposition Numbers 2478082−2478083 contain the supplementary crystallographic data for this paper. These data can be obtained free of charge via the joint Cambridge Crystallographic Data Centre (CCDC) and Fachinformationszentrum Karlsruhe Access Structures service.

## ■ AUTHOR INFORMATION


### Corresponding Author

**Ulrich Häussermann** − *Department of Chemistry, Stockholm University, SE-10691 Stockholm, Sweden;* orcid.org/0000-0003-2001-4410; Email: Ulrich.Haussermann@su.se

### Authors

**Doreen C. Beyer** − *Leipzig University, Faculty of Chemistry, Institute of Inorganic Chemistry and Crystallography, D-04103 Leipzig, Germany*

**Kristina Spektor** − *Deutsches Elektronen-Synchrotron DESY, D-22607 Hamburg, Germany;* orcid.org/0000-0002-3267-9797

**Roman Lucrezi** − *Department of Chemistry, Stockholm University, SE-10691 Stockholm, Sweden;* orcid.org/0000-0002-3117-3735

**Pedro Nunes Ferreira** − *Institute of Theoretical and Computational Physics, Graz University of Technology, NAWI Graz, 8010 Graz, Austria;* orcid.org/0000-0002-1135-0570

**Christoph Heil** − *Institute of Theoretical and Computational Physics, Graz University of Technology, NAWI Graz, 8010 Graz, Austria;* orcid.org/0000-0001-9693-9183

**Shrikant Bhat** − *Deutsches Elektronen-Synchrotron DESY, D-22607 Hamburg, Germany;* orcid.org/0000-0002-1229-9842

**Robert Farla** − *Deutsches Elektronen-Synchrotron DESY, D-22607 Hamburg, Germany*

**Volodymyr Baran** − *Deutsches Elektronen-Synchrotron DESY, D-22607 Hamburg, Germany;* orcid.org/0000-0003-2379-3632

**Martin Aaskov Karlsen** − *Deutsches Elektronen-Synchrotron DESY, D-22607 Hamburg, Germany;* orcid.org/0000-0003-1262-8965

**Martin Etter** − *Deutsches Elektronen-Synchrotron DESY, D-22607 Hamburg, Germany*

**Vanessa Stephan** − *Leipzig University, Faculty of Chemistry, Institute of Inorganic Chemistry and Crystallography, D-04103 Leipzig, Germany*

**Martin Boerner** − *Leipzig University, Faculty of Chemistry, Institute of Inorganic Chemistry and Crystallography, D-04103 Leipzig, Germany*

**Christopher Owen** − *School of Metallurgy and Materials, University of Birmingham, Birmingham B15 2TT, United Kingdom*

**Andrew J. Morris** − *School of Metallurgy and Materials, University of Birmingham, Birmingham B15 2TT, United Kingdom;* orcid.org/0000-0001-7453-5698

**Holger Kohlmann** − *Leipzig University, Faculty of Chemistry, Institute of Inorganic Chemistry and Crystallography, D-04103 Leipzig, Germany;* orcid.org/0000-0002-8873-525X

Complete contact information is available at: https://pubs.acs.org/10.1021/acs.chemmater.5c02061


### Notes

The authors declare no competing financial interest.

## ■ ACKNOWLEDGMENTS

This research has been supported by the Swedish Research Council (VR) through Project 2019-06063, by the German Research Foundation (DFG) through Project 277832266, and by the German Federal Ministry of Education and Research (BMBF) through Grant 05K20OLA. Beamline LVP instrument Aster-15 has been funded by the ErUM-Pro program of the BMBF (Grants 05K16WC2 and 05K13WC2). The authors are grateful to Per Mistenius for skillfully manufacturing the miniature press dies used for sample preparation. The computations were enabled by resources provided by the National Academic Infrastructure for Supercomputing in Sweden (NAISS), partially funded by the Swedish Research Council through Grant Agreement 2022-06725. DESY (Hamburg, Germany), a member of the Helmholtz Association HGF, is acknowledged for the provision of experimental facilities. Parts of this research were carried out at PETRA III

beamlines P61B and P02.1. Beamtime at P02.1 was allocated for Proposal I-20240035 and by an in-house contingent. Beamtimes at P61B were allocated for Proposals I-20211303 EC and I-20240358. R.L. acknowledges support from the Carl Tryggers foundation (CTS, Grant 23:2934), and P.N.F. acknowledges the São Paulo Research Foundation (FAPESP) under Grants 2020/08258-0 and 2021/13441-1. P.N.F. and C.H. acknowledge the computational resources of the dCluster of the Graz University of Technology and VSC5 of the Vienna Science Cluster (VSC). A.J.M gratefully acknowledges networking support from CCP-NC (UKRI grant EP/T026642/1, CCP9 (EP/T026375/1), and UKCP (EP/P022561/1) and C.O. acknowledges the ARCHER2 UK National Superconducting Service and the University of Birmingham's BlueBEAR HPC service for computational resources.

## REFERENCES

(1) Cava, R. J. Oxide Superconductors. *J. Am. Ceram. Soc.* **2000**, *83* (1), 5−28.
(2) Shaked, H. *Crystal Structures of the High-Tc Superconducting Copper-oxides: Physica: Superconductivity*; Elsevier, 1994.
(3) Paglione, J.; Greene, R. L. High-temperature superconductivity in iron-based materials. *Nat. Phys.* **2010**, *6* (9), 645−658.
(4) Tang, S.; Wu, M.; Bai, S.; Luo, D.; Zhang, J.; Wan, D.; Li, X. SnSe 2 monolayer with square lattice structure: a promising p-type thermoelectric material with an indirect bandgap and low lattice thermal conductivity. *J. Mater. Chem. C* **2022**, *10* (42), 16116−16125.
(5) Chen, X.; Deng, J.; Jin, S.; Ying, T.; Fei, G.; Ren, H.; Yang, Y.; Ma, K.; Yang, M.; Wang, J.; Li, Y.; Chen, X.; Liu, X.; Du, S.; Guo, J.-G.; Chen, X. Two-Dimensional Pb Square Nets from Bulk (RO)nPb (R = Rare Earth Metals, n = 1,2). *J. Am. Chem. Soc.* **2023**, *145* (31), 17435−17442.
(6) Klemenz, S.; Lei, S.; Schoop, L. M. Topological Semimetals in Square-Net Materials. *Annu. Rev. Mater. Res.* **2019**, *49* (1), 185−206.
(7) Klemenz, S.; Hay, A. K.; Teicher, S. M. L.; Topp, A.; Cano, J.; Schoop, L. M. The Role of Delocalized Chemical Bonding in Square-Net-Based Topological Semimetals. *J. Am. Chem. Soc.* **2020**, *142* (13), 6350−6359.
(8) Zagorac, D.; Müller, H.; Ruehl, S.; Zagorac, J.; Rehme, S. Recent developments in the Inorganic Crystal Structure Database: Theoretical crystal structure data and related features. *J. Appl. Crystallogr.* **2019**, *52* (5), 918−925.
(9) Orozco-Galvan, G. S.; García-Fuente, A.; Barraza-Lopez, S. Tight-binding model with sublattice-asymmetric spin-orbit coupling for square-net nodal line Dirac semimetals. *Phys. Rev. B* **2024**, *109* (3), No. 35141.
(10) Tremel, W.; Hoffmann, R. Square nets of main-group elements in solid-state materials. *J. Am. Chem. Soc.* **1987**, *109* (1), 124−140.
(11) A. Papoian, G.; Hoffmann, R. Hypervalent Bonding in One, Two, and Three Dimensions: Extending the Zintl-Klemm Concept to Nonclassical Electron-Rich Networks. *Angew. Chem., Int. Ed.* **2000**, *39* (14), 2408−2448.
(12) Ono, Y.; Hamano, T. Peierls Distortion in Two-Dimensional Tight-Binding Model. *J. Phys. Soc. Jpn.* **2000**, *69* (6), 1769−1776.
(13) Kushwaha, S. K.; Krizan, J. W.; Xiong, J.; Klimczuk, T.; Gibson, Q. D.; Liang, T.; Ong, N. P.; Cava, R. J. Superconducting properties and electronic structure of NaBi. *J. Phys.: Condens. Matter* **2014**, *26* (21), No. 212201.
(14) Górnicka, K.; Gutowska, S.; Winiarski, M. J.; Wiendlocha, B.; Xie, W.; Cava, R. J.; Klimczuk, T. Superconductivity on a Bi Square Net in LiBi. *Chem. Mater.* **2020**, *32* (7), 3150−3159.
(15) Morris, A. J.; Grey, C. P.; Pickard, C. J. Thermodynamically stable lithium silicides and germanides from density functional theory calculations. *Phys. Rev. B* **2014**, *90* (5), No. 54111.
(16) Zhang, S.; Wang, Y.; Yang, G.; Ma, Y. Silicon Framework-Based Lithium Silicides at High Pressures. *ACS Appl. Mater. Interfaces.* **2016**, *8* (26), 16761−16767.
(17) Evers, J.; Oehlinger, G.; Sextl, G. High-Pressure Synthesis of LiSi: Three-Dimensional Network of Three-Bonded Si − Ions. *Angew. Chem., Int. Ed. Engl.* **1993**, *32* (10), 1442−1444.
(18) Menges, E.; Hopf, V.; Schäfer, H.; Weiss, A. The Crystal Structure of LiGe—A New Three-Dimensional Unit of Group IV Elements. *Z. Naturforsch.* **1969**, *24B*, 1351−1352.
(19) Taubert, F.; Schwalbe, S.; Seidel, J.; Hüttl, R.; Gruber, T.; Janot, R.; Bobnar, M.; Gumeniuk, R.; Mertens, F.; Kortus, J. Thermodynamic characterization of lithium monosilicide (LiSi) by means of calorimetry and DFT-calculations. *Int. J. Mater. Res.* **2017**, *108* (11), 942−958.
(20) Tang, W. S.; Chotard, J.-N.; Janot, R. Synthesis of Single-Phase LiSi by Ball-Milling: Electrochemical Behavior and Hydrogenation Properties. *J. Electrochem. Soc.* **2013**, *160* (8), A1232−A1240.
(21) Stearns, L. A.; Gryko, J.; Diefenbacher, J.; Ramachandran, G. K.; McMillan, P. F. Lithium monosilicide (LiSi), a low-dimensional silicon-based material prepared by high pressure synthesis: NMR and vibrational spectroscopy and electrical properties characterization. *J. Solid State Chem.* **2003**, *173* (1), 251−258.
(22) Evers, J.; Oehlinger, G.; Sextl, G.; Becker, H.-O. High-Pressure LiGe with Layers Containing Two- and Four-Coordinate Germanium Atoms. *Angew. Chem., Int. Ed. Engl.* **1987**, *26* (1), 76−78.
(23) Evers, J.; Oehlinger, G. Isolated Hexagonal Channels Built up by Three-Connected Ge− Ions in LiGe at High Pressure. *Angew. Chem., Int. Ed.* **2001**, *40* (6), 1050−1053.
(24) Schwarzmüller, S.; Jakob, M.; Nentwig, M.; Schröder, T.; Kuhn, A.; Düvel, A.; Heitjans, P.; Oeckler, O. Tuning the Vacancy Concentration in Lithium Germanium Antimony Tellurides—Influence on Phase Transitions, Lithium Mobility, and Thermoelectric Properties. *Chem. Mater.* **2018**, *30* (21), 7970−7978.
(25) von Schnering, H. G.; Nesper, R.; Curda, J.; Tebbe, K.-F. Li12Si7, a Compound Having a Trigonal Planar Si4 Cluster and Planar Si5 Rings. *Angew. Chem., Int. Ed.* **1980**, *19* (12), 1033−1034.
(26) Thomas, D.; Abdel-Hafiez, M.; Gruber, T.; Hüttl, R.; Seidel, J.; Wolter, A. U.; Büchner, B.; Kortus, J.; Mertens, F. The heat capacity and entropy of lithium silicides over the temperature range from (2 to 873)K. *J. Chem. Thermodyn.* **2013**, *64*, 205−225.
(27) Farla, R.; Bhat, S.; Sonntag, S.; Chanyshev, A.; Ma, S.; Ishii, T.; Liu, Z.; Néri, A.; Nishiyama, N.; Faria, G. A.; Wroblewski, T.; Schulte-Schrepping, H.; Drube, W.; Seeck, O.; Katsura, T. Extreme conditions research using the large-volume press at the P61B endstation, PETRA III. *J. Synchrotron Radiat.* **2022**, *29* (2), 409−423.
(28) Vekilova, O. Y.; Beyer, D. C.; Bhat, S.; Farla, R.; Baran, V.; Simak, S. I.; Kohlmann, H.; Häussermann, U.; Spektor, K. Formation and Polymorphism of Semiconducting K2SiH6 and Strategy for Metallization. *Inorg. Chem.* **2023**, *62* (21), 8093−8100.
(29) Matsui, M.; Higo, Y.; Okamoto, Y.; Irifune, T.; Funakoshi, K.-I. Simultaneous sound velocity and density measurements of NaCl at high temperatures and pressures: Application as a primary pressure standard. *Am. Mineral.* **2012**, *97* (10), 1670−1675.
(30) Seto, S.; Nishio-Hamane, D.; Nagai, T.; Sata, N. Development of a software suite on X-ray diffraction experiments. *Rev. High Press. Sci. Technol.* **2010**, *20*, 269−276.
(31) Taupin, D. A powder-diagram automatic-indexing routine. *J. Appl. Crystallogr.* **1973**, *6* (5), 380−385.
(32) Shirley, R. *Crysfire 2004: An interactive powder indexing support system*; 2004.
(33) Le Bail, A.; Duroy, H.; Fourquet, J. L. Ab-initio structure determination of LiSbWO6 by X-ray powder diffraction. *Mater. Res. Bull.* **1988**, *23* (3), 447−452.
(34) Toby, B. H.; Von Dreele, R. B. GSAS-II: the genesis of a modern open-source all purpose crystallography software package. *J. Appl. Crystallogr.* **2013**, *46* (2), 544−549.
(35) Dippel, A.-C.; Liermann, H.-P.; Delitz, J. T.; Walter, P.; Schulte-Schrepping, H.; Seeck, O. H.; Franz, H. Beamline P02.1 at


https://doi.org/10.1021/acs.chemmater.5c02061
*Chem. Mater.* XXXX, XXX, XXX−XXX

PETRA III for high-resolution and high-energy powder diffraction. *J. Synchrotron Radiat.* **2015**, *22* (3), 675−687.
(36) Rodríguez-Carvajal, J., Ed. *FULLPROF (version 5.20): A Program for Rietveld Refinement and Pattern Matching Analysis*; Insitut Laue-Langevin: Grenoble, France, 2012.
(37) Giannozzi, P.; Baroni, S.; Bonini, N.; Calandra, M.; Car, R.; Cavazzoni, C.; Ceresoli, D.; Chiarotti, G. L.; Cococcioni, M.; Dabo, I.; Dal Corso, A.; de Gironcoli, S.; Fabris, S.; Fratesi, G.; Gebauer, R.; Gerstmann, U.; Gougoussis, C.; Kokalj, A.; Lazzeri, M.; Martin-Samos, L.; Marzari, N.; Mauri, F.; Mazzarello, R.; Paolini, S.; Pasquarello, A.; Paulatto, L.; Sbraccia, C.; Scandolo, S.; Sclauzero, G.; Seitsonen, A. P.; Smogunov, A.; Umari, P.; Wentzcovitch, R. M. QUANTUM ESPRESSO: a modular and open-source software project for quantum simulations of materials. *J. Phys.: Condens. Matter* **2009**, *21* (39), No. 395502.
(38) Giannozzi, P.; Andreussi, O.; Brumme, T.; Bunau, O.; Buongiorno Nardelli, M.; Calandra, M.; Car, R.; Cavazzoni, C.; Ceresoli, D.; Cococcioni, M.; Colonna, N.; Carnimeo, I.; Dal Corso, A.; de Gironcoli, S.; Delugas, P.; DiStasio, R. A.; Ferretti, A.; Floris, A.; Fratesi, G.; Fugallo, G.; Gebauer, R.; Gerstmann, U.; Giustino, F.; Gorni, T.; Jia, J.; Kawamura, M.; Ko, H.-Y.; Kokalj, A.; Küçükbenli, E.; Lazzeri, M.; Marsili, M.; Marzari, N.; Mauri, F.; Nguyen, N. L.; Nguyen, H.-V.; Otero-de-la-Roza, A.; Paulatto, L.; Poncé, S.; Rocca, D.; Sabatini, R.; Santra, B.; Schlipf, M.; Seitsonen, A. P.; Smogunov, A.; Timrov, I.; Thonhauser, T.; Umari, P.; Vast, N.; Wu, X.; Baroni, S. Advanced capabilities for materials modelling with Quantum ESPRESSO. *J. Phys.: Condens. Matter* **2017**, *29* (46), No. 465901.
(39) Giannozzi, P.; Baseggio, O.; Bonfà, P.; Brunato, D.; Car, R.; Carnimeo, I.; Cavazzoni, C.; de Gironcoli, S.; Delugas, P.; Ferrari Ruffino, F.; Ferretti, A.; Marzari, N.; Timrov, I.; Urru, A.; Baroni, S. Quantum ESPRESSO toward the exascale. *J. Chem. Phys.* **2020**, *152* (15), No. 154105.
(40) Baroni, S.; de Gironcoli, S.; Dal Corso, A.; Giannozzi, P. Phonons and related crystal properties from density-functional perturbation theory. *Rev. Mod. Phys.* **2001**, *73* (2), 515−562.
(41) Hamann, D. R. Optimized norm-conserving Vanderbilt pseudopotentials. *Phys. Rev. B* **2013**, *88* (8), No. 85117.
(42) Schlipf, M.; Gygi, F. Optimization algorithm for the generation of ONCV pseudopotentials. *Comput. Phys. Commun.* **2015**, *196*, 36−44.
(43) Perdew, J. P.; Burke, K.; Ernzerhof, M. Generalized Gradient Approximation Made Simple. *Phys. Rev. Lett.* **1996**, *77* (18), 3865−3868.
(44) Methfessel, M.; Paxton, A. T. High-precision sampling for Brillouin-zone integration in metals. *Phys. Rev. B* **1989**, *40* (6), 3616−3621.
(45) Kogler, E.; Spath, D.; Lucrezi, R.; Mori, H.; Zhu, Z.; Li, Z.; Margine, E. R.; Heil, C. IsoME: Streamlining High-Precision Eliashberg Calculations. *Comput. Phys. Commun.* **2025**, *315*, No. 109720.
(46) Morel, P.; Anderson, P. W. Calculation of the Superconducting State Parameters with Retarded Electron-Phonon Interaction. *Phys. Rev.* **1962**, *125* (4), 1263−1271.
(47) Lucrezi, R.; Ferreira, P. P.; Hajinazar, S.; Mori, H.; Paudyal, H.; Margine, E. R.; Heil, C. Full-bandwidth anisotropic Migdal-Eliashberg theory and its application to superhydrides. *Commun. Phys.* **2024**, *7* (1), 1−13.
(48) Otero-de-la-Roza, A.; Blanco, M. A.; Pendás, A. M.; Luaña, V. Critic: a new program for the topological analysis of solid-state electron densities. *Comput. Phys. Commun.* **2009**, *180* (1), 157−166.
(49) Otero-de-la-Roza, A.; Johnson, E. R.; Luaña, V. Critic2: A program for real-space analysis of quantum chemical interactions in solids. *Comput. Phys. Commun.* **2014**, *185* (3), 1007−1018.
(50) Yu, M.; Trinkle, D. R. Accurate and efficient algorithm for Bader charge integration. *J. Chem. Phys.* **2011**, *134* (6), No. 64111.
(51) Henkelman, G.; Arnaldsson, A.; Jónsson, H. A fast and robust algorithm for Bader decomposition of charge density. *Comput. Mater. Sci.* **2006**, *36* (3), 354−360.
(52) Sanville, E.; Kenny, S. D.; Smith, R.; Henkelman, G. Improved grid-based algorithm for Bader charge allocation. *J. Comput. Chem.* **2007**, *28* (5), 899−908.
(53) Tang, W.; Sanville, E.; Henkelman, G. A grid-based Bader analysis algorithm without lattice bias. *J. Phys.: Condens. Matter* **2009**, *21* (8), No. 084204.
(54) Momma, K.; Izumi, F. VESTA 3 for three-dimensional visualization of crystal, volumetric and morphology data. *J. Appl. Crystallogr.* **2011**, *44* (6), 1272−1276.
(55) Kresse, G.; Joubert, D. From ultrasoft pseudopotentials to the projector augmented-wave method. *Phys. Rev. B* **1999**, *59* (3), 1758−1775.
(56) Dal Corso, A. Pseudopotentials periodic table: From H to Pu. *Comput. Mater. Sci.* **2014**, *95*, 337−350.
(57) Becke, A. D.; Edgecombe, K. E. A simple measure of electron localization in atomic and molecular systems. *J. Chem. Phys.* **1990**, *92* (9), 5397−5403.
(58) Bader, R. F. W. *Atoms in Molecules: A Quantum Theory*; Oxford University Press, 1990.
(59) Gatti, C. Chemical bonding in crystals: New directions. *Z. Kristallogr. Cryst. Mater.* **2005**, *220* (5−6), 399−457.
(60) Grin, Y.; Savin, A.; Silvi, B. The ELF Perspective of chemical bonding. In *The Chemical Bond*; John Wiley & Sons, Ltd., 2014; pp 345−382.
(61) Setyawan, W.; Curtarolo, S. High-throughput electronic band structure calculations: Challenges and tools. *Comput. Mater. Sci.* **2010**, *49* (2), 299−312.




https://doi.org/10.1021/acs.chemmater.5c02061
Chem. Mater. XXXX, XXX, XXX−XXX